Applied Physics A (2022) 128:328
https://doi.org/10.1007/s00339-022-05495-z

Applied Physics A
Materials Science & Processing

The optical, electrical and mechanical performance of metal oxides incorporated PVA/rGO blend: effect of metal oxide type

Ali Badawi[1,2] · **Sami S. Alharthi**[1]

Received: 9 February 2022 / Accepted: 15 March 2022 / Published online: 21 March 2022

Abstract

The effect of metal (M: Fe, Pb and Mn) oxides type on the optical, electrical and mechanical performance of PVA/reduced graphene oxide (PVA/rGO) blend has been explored. Plain PVA and 2.0 wt% of metal oxides polymeric composites (PCs) were equipped using the solution casting procedure. The structure variation due to metal oxides incorporation was examined by the FT-IR spectroscopy. The optical properties of the samples were obtained based on the UV–Vis–NIR measurements. The optical bandgap decreases from 5.41 eV (plain PVA) to 5.36 eV (plain PVA/rGO), 5.23 eV (Fe_2O_3 PC), 5.27 eV (Pb_3O_4 PC) and 5.22 eV (MnO_2 PC). The dc-electrical conductivity of the PVA/rGO blend is strongly enhanced via metal oxides incorporation. The activation energy of the host matrix decreases from 0.66 eV (plain PVA) to 0.18 eV (plain PVA/rGO), 0.05 eV (Fe_2O_3 PC), 0.20 eV (Pb_3O_4 PC) and 0.43 eV (MnO_2 PC). The dynamic mechanical analyzer (DMA) was used to investigate the effect of metal oxides incorporation on the mechanical properties of the host blend. The glass transition temperature (T_g) value increases from 59.45 °C (plain PVA) to 61.56 °C (plain PVA/rGO) and 64.68 °C (Pb_3O_4 PC). While it decreases to 55.04 °C (Fe_2O_3 PC) and 58.37 °C (MnO_2 PC). These unique results exhibit that the optical, electrical and mechanical properties of polymeric blends could be controlled via metal oxides incorporation for applications in flexible optoelectronic devices.

Keywords Metal oxides incorporation · PVA/reduced graphene oxide · Optical · Electrical · Mechanical · Flexible optoelectronic devices

1 Introduction

In the last two decades, a researches trend has been focusing on polymer composites (PCs) due to their possible participations in many daily fields [1–4]. This scientific concern of PCs arises owing to their unique characteristics including lightweight, flexibility, availability and relatively low cost [5–9]. In addition, polymers' features qualify them to act the hosts' role for various kinds of fillers. PCs could be made to meet such an application in optoelectronics, shielding, optical devices, photocatalysts, sensors, solar cells, supercapacitors and medicine [4, 10–13]. Specifically, PCs based on polyvinyl alcohol (PVA) as a host matrix are given superior attention due to PVA's unique physical and chemical characteristics. These characteristics include its high optical transmittance in the visible–NIR region, wide bandgap (~ 5.3 eV [14]) and semi crystallinity nature. The last feature arises due to the existence of the hydroxyl (OH) group in its chains which qualify it as an ideal host for a lot of fillers [5, 15, 16]. Besides, its biodegradable, water-soluble and friendly environmental features introduce it for a wide range of applications [14, 17, 18]. Moreover, the ability of blending PVA with such an amorphous polymer or a crystalline material is easy to be performed for multiple industrial applications. Carbon derivatives are promising over a lot of material to be blended with the PVA polymer to form a new kind of host materials. Reduced graphene oxide (rGO) is one of these carbon derivatives that is favorable because of its novel mechanical and electrical properties. Moreover, its excessive hardness and lightweight provide the principal host (PVA) more preferable features to the produced blend [19–24]. It is worth mentioning that rGO is optimized over other carbon derivatives to form polymeric blends since its

✉ Ali Badawi
daraghmeh@tu.edu.sa

[1] Department of Physics, College of Science, Taif University, P.O. Box 11099, Taif 21944, Saudi Arabia

[2] Department of Physics, University College of Turabah, Taif University, P.O. Box 11099, Taif 21944, Saudi Arabia

high electrical conductivity, virtuous ability to materials interaction and high mobility [25, 26].

A lot of reported works in the literature concerned the PVA modification and its blends. Aslam group explored the effect of graphene oxide on the structural and opto-mechanical performance of PVA for opto-electronic devices [27]. They found that Young's modulus and tensile strength of the prepared blend were entirely enhanced. Mahendia et al. used rGO to enhance the thermal performance as well as the glass transition temperature of PVA [28]. The optical bandgap of PVA was tuned using multi-walled CNTs by Zidan researches group [29]. Furthermore, the electrical conductivity of PVA was greatly improved by blending it with GO for electronic applications [20]. In addition, the mechanical properties of PVA were reinforced by graphene for antibacterial applications [30]. Besides, a lot of previous works explored the effect of the metal oxides weight ratio on the different functional properties of PVA in the literature [31–33]. The optical and structural performance of PVA was tailored by blending with different weight ratios of iron oxide [31]. Khairy research group controlled the optical characteristics of PVA by ZrO_2 incorporation for UV-block applications [33]. Alrowiali et al. concluded that the optical parameter of PVA could be enhanced significantly by Y_2O_3 embedding [32]. In our previous work, we found that PVA blended with graphene is an ideal host for FeS nanoparticles for eco-environmentally applications [13].

The current work aims to explore the effect of metal oxides' type (M: Fe, Pb and Mn oxides) on the optical, electrical and mechanical performance of PVA/rGO blend. To the best of our knowledge, such a comparative study on the functional properties of PVA/rGO PCs has not been reported before. Metal oxides are selected to play this role, since their semiconducting feature allows to tailor the optical, mechanical and electrical properties of PVA/rGO blend in a wide range for various applications**.** Moreover, their unique properties as availability and low cost are also welcomed. In this work, factors such as concentration, thickness, preparation conditions, etc. that may affect the functional performance of the host PVA/rGO blend are fixed, while the effect of the filler's type (metal oxides) is explored. The bonds' vibrations, optical, electrical and mechanical performance of the metal oxides incorporated PVA/rGO blend are obtained from the Fourier transform infrared (FT-IR), UV–Vis–NIR, four-probe method and dynamic mechanical analyzer (DMA) measurements, respectively. In addition, the surface morphology of the PCs were analyzed based on scanning electron microscope examinations.

2 Methods and materials

Many raw materials are required to prepare the plain PVA and metal oxides incorporated PVA/rGO PCs, as listed in Table 1. No further purification was performed on the purchased materials. The solution casting procedure described by Heiba et al. was followed to prepare the plain and incorporated PCs [34]. First, 10 g of PVA granules were dissolved in 250 ml of double-distilled water at 70 °C with continuous stirring for 3 h to obtain a clear solution. Second, 50 ml of the previous solution was taken off to prepare the plain PVA sample. Third, 0.1 wt% of rGO/PVA blend was prepared by adding the required weight of rGO nanosheets into the previous PVA solution. With a magnetic stirring for 24 h at room temperature, a homogenous blend of PVA/rGO was achieved. Fourth, another 50 ml of the blend were taken off to prepare the plain PVA/rGO sample. Fifth, the remaining PVA/rGO blend was divided into three parts to obtain the metal oxide-incorporated PVA/rGO PCs by adding 2.0 wt% of the metal oxide into the previous PVA/rGO blend with stirring for 3 h to obtain the homogenous PC. Sixth, the previous five solutions were poured in glassy Petri dishes and put in an oven at 55 °C for 48 h. After that, the samples were left to reach the room temperature. Five films with three specimens of each with thicknesses of 0.20 mm ± 0.01 mm were obtained and marked (S_1 to S_5) to perform the examinations.

The surfaces' morphology of the unincorporated and metal oxides incorporated PVA/rGO blend was captured using a scanning electron microscope (JOEL, Model: 3600 LA). The structure's variation of the samples was examined via FT-IR measurements using a Shimadzu (IRAffinity-1S) spectrophotometer over wavenumbers ranging from 400 to 4000 cm^{-1}. The optical properties were obtained from the analysis of the

Table 1 Materials used in the current study

Material	Conditions	Supplier
Ferric (III) oxide (Fe_2O_3)	Purity ≥ 96%	Sigma-Aldrich Co
Lead (II,IV) oxide (Pb_3O_4)	Purity ≥ 99%	Sigma-Aldrich Co
Manganese oxide (MnO_2)	Purity ≥ 99%	Sigma-Aldrich Co
reduced graphene oxide (rGO) nano sheets	Thickness:0.55–3.74 nm, Purity ≥ 98%	Chengdu organic chemicals
PVA	(86–89% hydrolyzed, M.W.: 850,000 $g.mol^{-1}$	Alfa Aesar

UV–visible–NIR absorbance (A) and transmittance (T) spectra measurements measured by a JASCO (V-670) spectrophotometer with three-time rounds to confirm the reproducibility of the obtained data. The main linear optical parameters: optical absorption coefficient (α), extinction coefficient (K), reflectance ($\mathcal{R}$), energy bandgap (E_g), Urbach energy (E_u), refractive index (n) and real (ε_r) and imaginary (ε_i) dielectric constants of the samples were determined using the following equations [35–44]:

$$\alpha = \frac{2.303A}{d} \tag{1}$$

$$\alpha h\nu = B\left(h\nu - E_g\right)^m \tag{2}$$

$$\alpha = \alpha_0 \exp\left(h\nu/E_u\right) \tag{3}$$

$$n = \left(\frac{1+\mathcal{R}}{1-\mathcal{R}}\right) + \left[\frac{4\mathcal{R}}{(1-\mathcal{R})^2} - K^2\right]^{1/2} \tag{4}$$

$$K = \frac{\alpha\lambda}{4\pi} \tag{5}$$

$$\mathcal{R} = 1 - \sqrt{T \times e^A} \tag{6}$$

$$\varepsilon_r = n^2 - K^2 \tag{7}$$

$$\varepsilon_i = 2nK, \tag{8}$$

where d is the sample's thickness, B is a constant, α_0 is a constant and $h\nu$ is photons energy. While m parameter relates to the electronic transition type (direct ($m=0.5$) and indirect ($m=2$)).

Besides, the Wemple–DiDomenico (W–D) and Sellmeier oscillator models were used to examine the refractive index at infinity (n_∞), energy dispersion parameters (E_0 and E_d), average inter-band oscillator wavelength (λ_0), average oscillator strength (S_0), infinite dielectric constant (ε_∞), lattice dielectric constant (ε_L), free carrier concentration to the effective mass ratio (N/m*) and the plasma frequency (ω_p) from [9, 45]

$$n^2 = 1 + \frac{E_d E_0}{E_0^2 - (h\nu)^2} \tag{9}$$

$$\frac{n_\infty^2 - 1}{n^2 - 1} = 1 - \left(\frac{\lambda_0}{\lambda}\right)^2 \tag{10}$$

$$\left(n^2 - 1\right)^{-1} = \frac{1 - \left(\frac{\lambda_0}{\lambda}\right)^2}{S_0 \lambda_0^2} \tag{11}$$

$$S_0 = \frac{n_\infty^2 - 1}{\lambda_0^2} \tag{12}$$

$$\varepsilon_\infty = n_\infty^2 \tag{13}$$

$$\varepsilon_r = n^2 = \varepsilon_L - \frac{e^2}{4\pi^2 C^2 \varepsilon_0}\frac{N}{m^*}\lambda^2 \tag{14}$$

$$\omega_p = \left(\frac{e^2 N}{\pi C^2 m^*}\right)^{1/2}, \tag{15}$$

where λ, C, e and ε_0 are incident wavelength, speed of light, free-electron charge and space dielectric constant, respectively.

The dc electrical resistance (R) performance was measured by a four-probe stage under temperature (T) sweeping rate of 1 K/min from 300 to 400 K via an Oxfored Optistat cryostat. Keithley sourcemeter (model: 6517B) was used to record the current–voltage curves. All electrical resistance measurements were performed three-time rounds. The activation energy (E_a) of the prepared PCs was deduced using the Arrhenius relation given as [5, 46]

$$\sigma_{dc} = \sigma_0 \exp\left(E_a/\left(K_B T\right)\right), \tag{16}$$

where K_B and σ_0 are the Boltzman constant and pre-exponential factor, respectively.

The dynamic mechanical properties: storage modulus (E'), loss modulus (E''), stiffness and loss factor ($\mathrm{Tan}\delta = \frac{E''}{E'}$) ([47]) are measured using a dynamic mechanical analyzer (DMA, Q800). A static force of 0.01 N, strain amplitude of 15 µm and frequency of 1 Hz was applied through temperature sweeping from 30 to 120 °C and a rate of 3 °C/min. Three-time rounds were performed to ensure the reproducibility of the obtained mechanical measurements.

3 Results and discussion

3.1 Surface morphology analysis

Figure 1a–d shows the captured surfaces' morphology of the unincorporated and metal oxides incorporated PVA/rGO PCs surfaces using a scanning electron microscope (SEM). First, SEM micrographs confirm that all PCs are pinhole-free. In addition, SEM micrograph of the unincorporated PVA/rGO blend (Fig. 1a) reveals its smoothness without

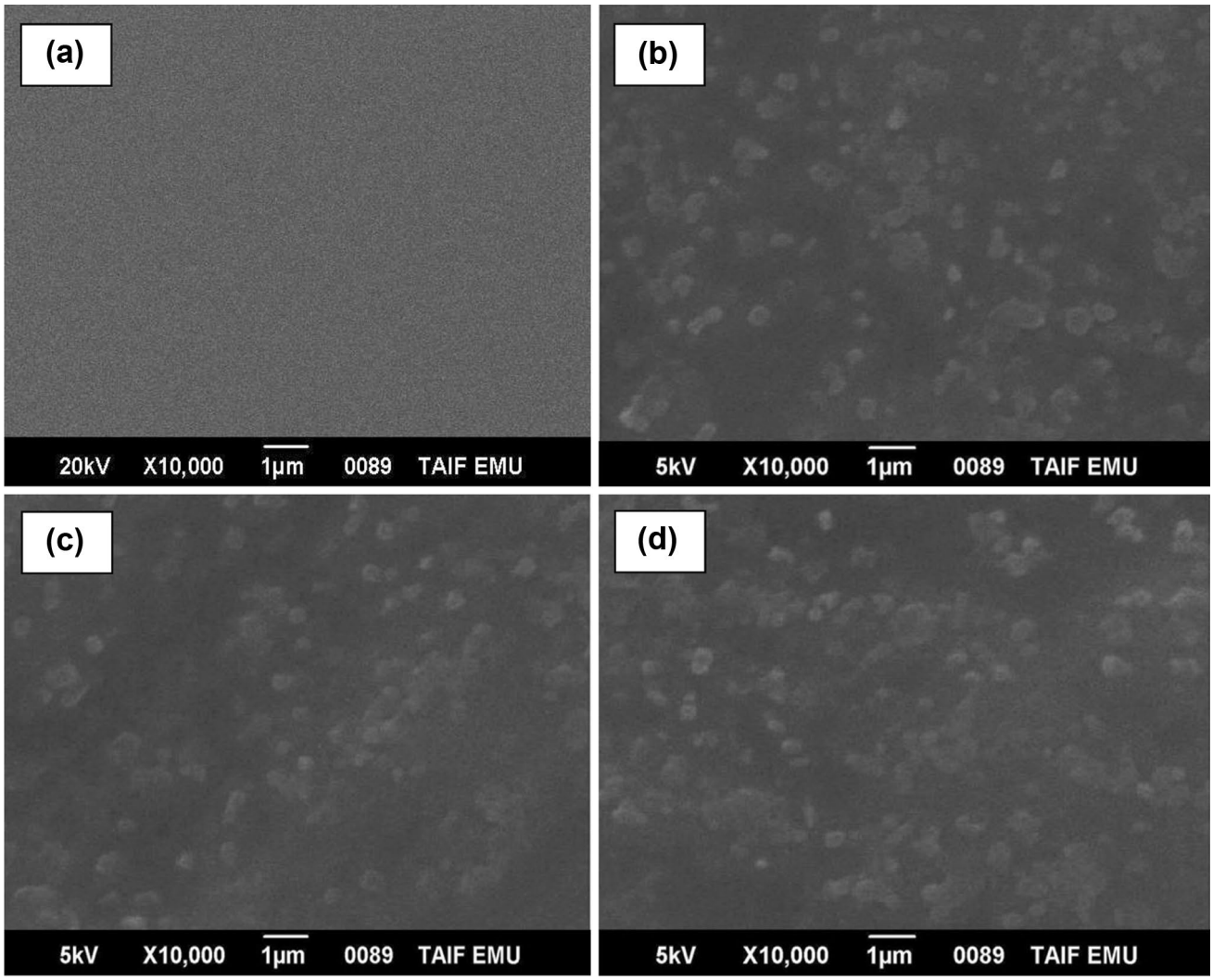

Fig. 1 SEM micrographs of **a** unincorporated and metal (M: Fe, Pb, Mn; (**b**–**d**)) oxides incorporated PCs, respectively

any impurities. While the SEM micrographs of the metal oxides incorporated PVA/rGO PCs (Fig. 1b–d) reveal the existence of well-distributed bright spots pinned in the host matrix. In addition, the SEM micrographs of metal oxides incorporated PCs seem more roughness as compared with the unincorporated blend.

3.2 FT-IR analysis

The variations in the PVA and PVA/rGO blend structures due to the metal oxides incorporation have been examined using FT-IR spectroscopy. Figure 2a displays the FT-IR transmittance spectra of the plain PVA, metal (M: Fe, Pb, Mn) oxides incorporated and unincorporated PVA/rGO blend in the wavenumber range from 400 to 4000 cm^{-1}. Based on the FT-IR spectrum of the plain PVA, the locations of the observed absorption bands and their corresponding bonds' vibration are listed in Table 2. As compared with the plain PVA FT-IR spectrum, two additional small absorption peaks located at 1636 cm^{-1} and 1542 cm^{-1} are detected in the FT-IR spectra of the incorporated and unincorporated PCs. These absorption peaks result due to the rGO blending and correspond to the vibrations of O–H bending and C=C, respectively [8, 27]. In addition, a tiny absorption peak centered at 3740 cm^{-1} relates to the stretching of the hydroxyl group (OH) on adsorbed on the rGO sheets [48]. While the metal oxides incorporation effect on the structure of PVA/rGO blend is clearly noticed in the wavenumber range from 650 to 400 $cm^{-1,}$ as depicted in Fig. 2b. These additional absorption peaks as well as the variation in the absorption intensities are attributed to the M–O (M: Fe, Pb, Mn) bonds torsional and stretching vibrations [49–51]. Moreover, slight shifts in peaks' location to lower wavenumbers of the host

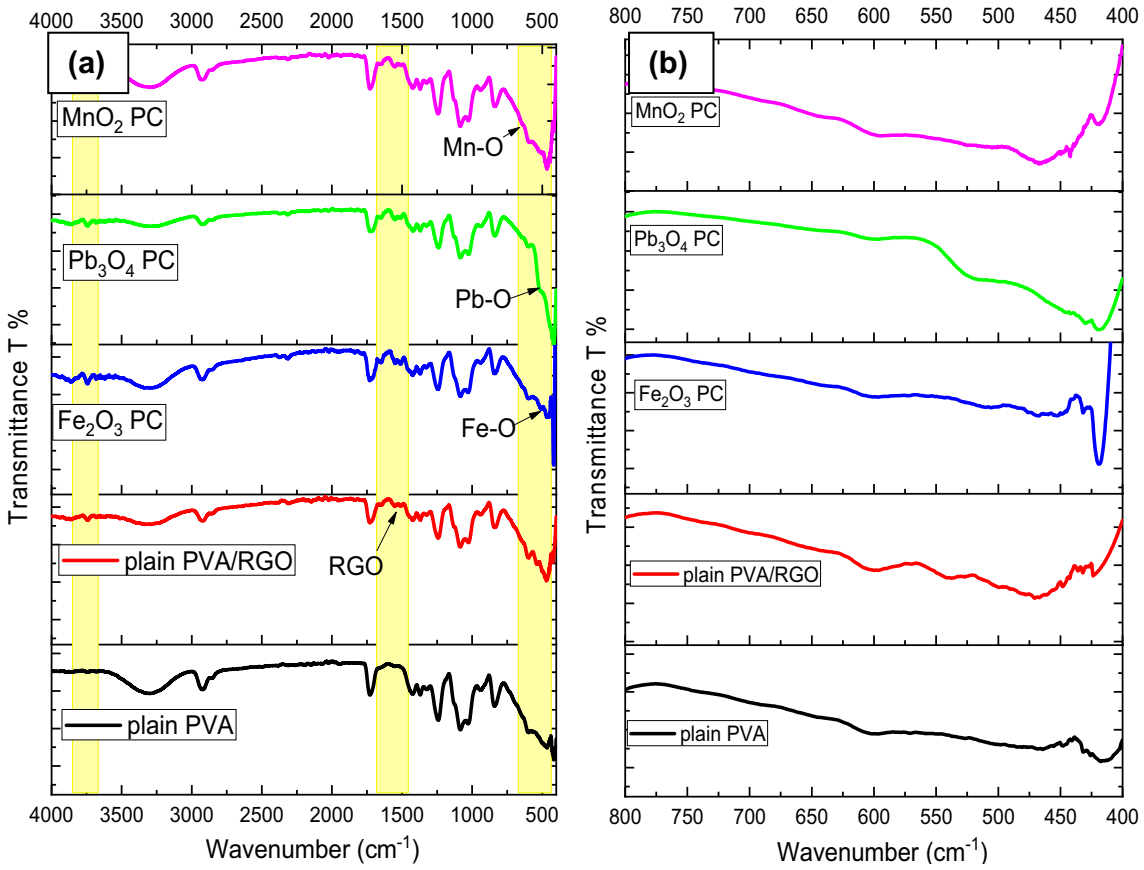

Fig. 2 FT-IR transmittance spectra of plain PVA and metal (M: Fe, Pb, Mn) oxides PCs vs. wavenumbers range from **a** 4000 to 400 cm^{-1} and **b** 800 to 400 cm^{-1}

Table 2 Absorption band locations and their corresponding bonds' vibrations of plain PVA and metal (M: Fe, Pb, Mn) oxides incorporated and unincorporated PVA/rGO blends

Absorption band location (cm^{-1})	Corresponding bond's vibration	References
Broad 3065—3556	Stretching of OH	[7, 55]
2925	Asymmetric stretching of CH	[29, 56]
1726	Stretching of C=O	[57, 58]
1423	Symmetric bending of CH_2	[29, 59]
1370	Wagging of C–H	[59]
1242	Stretching of C–C	[59]
1088	Stretching of C–O	[29]
1015	Bending of O–H	[60]
930	Rocking of CH_2	[29]
840	Stretching of C–C	[61]
629	Stretching of C–H	[56]

blend are detected which emphasize the positive interaction between the filler (metal oxide) and the host blend. These interactions in the blend' structure lead to clear modifications in the optical, mechanical and electrical performance of the PVA/rGO blend as discussed below. Similar findings were reported in the literature [52–54].

3.3 UV–visible–NIR analysis

Exploring the optical performance of the prepared films is significant to determine their suitability in such an optoelectronic application. The absorbance (*A*) and transmittance (*T*) spectra of the plain PVA and metal (M: Fe, Pb, Mn) oxides PCs in the UV–Vis–NIR regions are illustrated in Fig. 3a, b, respectively. All absorption spectra of the prepared films exhibit two absorption peaks at 211 nm and 278 nm that resemble the $\pi \rightarrow \pi^*$ inter-band electronic transitions of PVA [62, 63]. In addition, an absorption edge at 332 nm is also observed which corresponds to the $n \rightarrow \pi^*$ electronic transition of PVA [64]. As compared with the plain PVA spectrum, no additional peaks are noted in the metal oxides PCs. In addition, the absorption amount increases and hence the transmittance decreases due to the incorporation process. Moreover, the Fe_2O_3 PC film exhibits the largest absorption in the UV–Vis region, while the MnO_2 one exhibits the smallest one in the indicated region. The vice versa

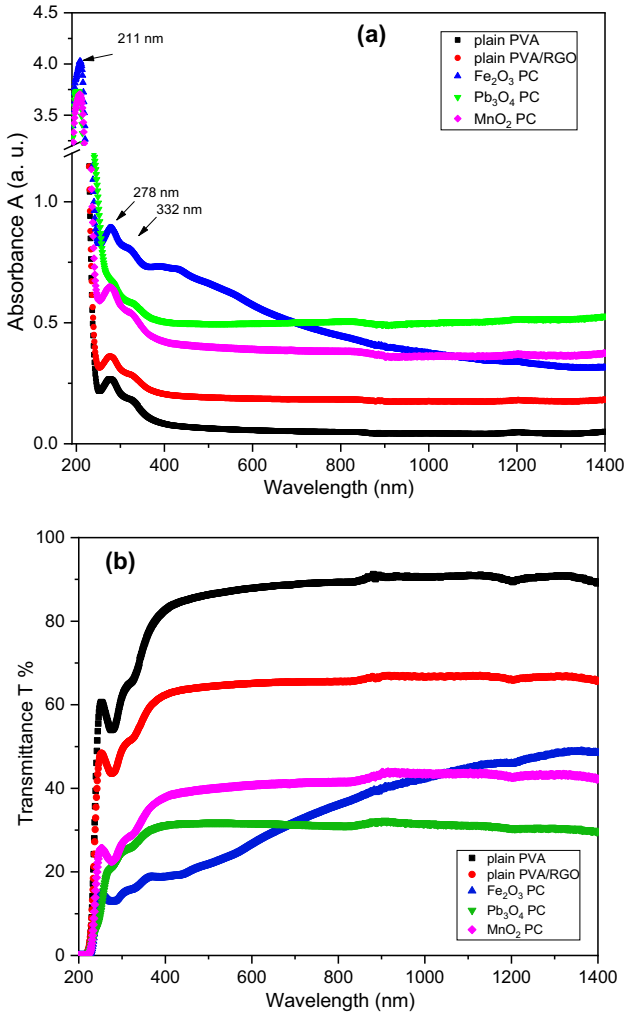

Fig. 3 Absorbance and transmittance of plain PVA and metal (M: Fe, Pb, Mn) oxides PCs vs. wavelength

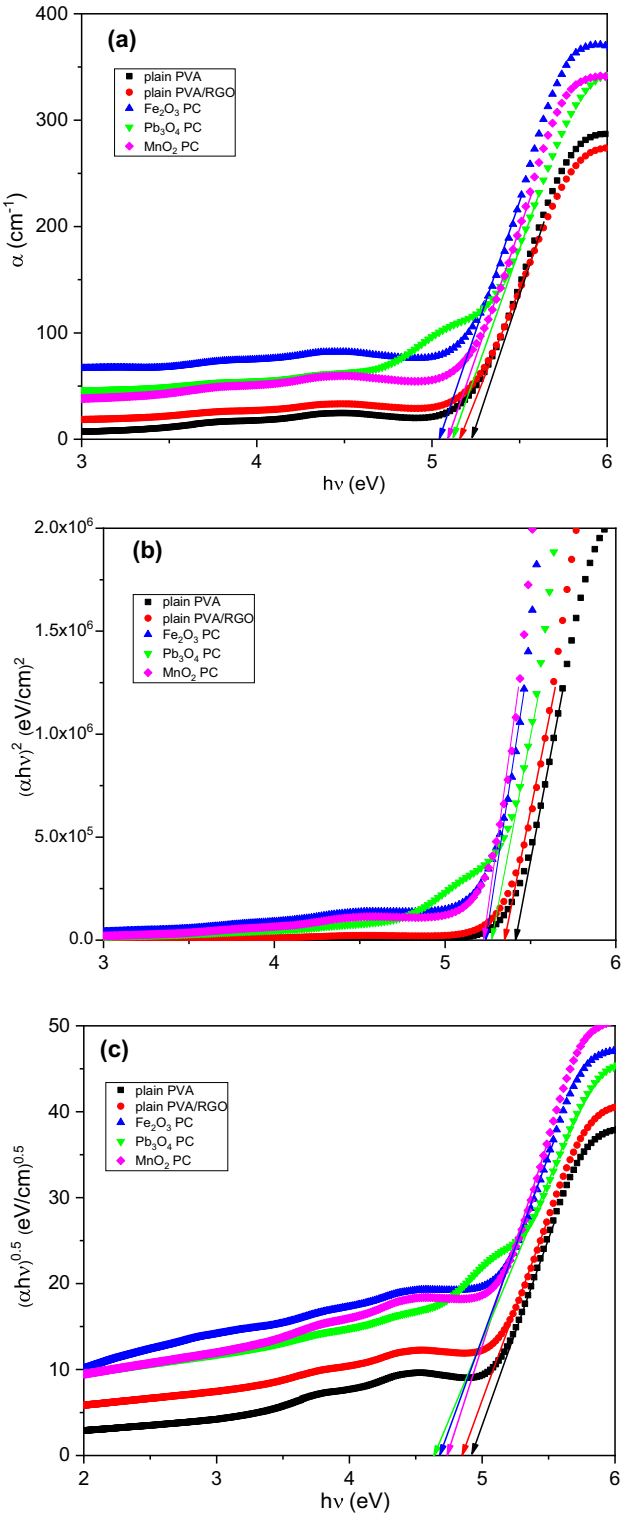

Fig. 4 **a** Absorption coefficient, **b** direct and **c** indirect Tauc's plot of plain PVA and metal PCs vs. $h\nu$

behaviour is noticed in the transmittance spectra of the samples. For example, at $\lambda = 600$ nm, T of the plain PVA is 88% and decreases to 65% (plain PVA/rGO), 41% (MnO_2 PC), 32% (Pb_3O_4 PCA) and 27% (Fe_2O_3 PC). This variation in the absorption and transmittance spectra is attributed to the variations in the optical bandgap of prepared films. This differentiation in the optical absorption and hence the transmittance due to varying the filler's type gives additional opportunities for new optical and optoelectronic applications.

The effect of the metal oxides incorporation on the optical absorption coefficient (α) and energy bandgap (E_g) of the PVA/rGO blend has been explored. Figure 4a presents α plots of plain PVA and metal (M: Fe, Pb, Mn) oxides PCs as a function of incident photons energy ($h\nu$). The obtained energy bandgap from the absorbance measurements ($E_{g\ Abs.}$) of the prepared PCs are listed in Table 3. According to Fig. 4, all films absorb significantly the UV spectrum, while their absorption decrease in both the visible-NIR spectra. In addition, red-shifts of the absorption edge of the PCs with respect to the plain one. The obtained $E_{g\ Abs}$ value of plain PVA is 5.23 eV which is consistent with reported values [32,

Table 3 E_g (in eV) and E_u values of metal oxides PCs

Sample	$E_{g\ Abs}$	$E_{g\ d}$	$E_{g\ ind}$	$E_{g\ ei}$	E_u (eV)
Plain PVA PVP/PVA	5.23	5.41	4.92	5.42	0.21
Plain PVA/rGO	5.16	5.36	4.85	5.35	0.28
Fe_2O_3 PC	5.04	5.23	4.68	5.23	0.41
Pb_3O_4 PC	5.13	5.27	4.64	5.31	0.64
MnO_2 PC	5.09	5.22	4.73	5.27	0.34

65]. Moreover, Fe_2O_3 PC possesses the lowest $E_{g\ Abs}$ value (5.04 eV), while Pb_3O_4 PC has the highest one (5.13 eV). The variation in the $E_{g\ Abs}$ values is attributed to defects' creations as a result of the incorporation process.

Furthermore, Tauc's relation (Eq. 2) is used to determine the direct ($m = 1/2$) and indirect ($m = 2$) optical bandgap of the prepared films. To perform that, $(\alpha h\nu)^2$ and $(\alpha h\nu)^{0.5}$ values of the plain PVA and incorporated and unincorporated PCs as a function of hν are plotted, as depicted in Fig. 4b, c, respectively. The obtained E_g values are tabulated in Table 3. It is noticed that the E_g value of the plain PVA decreases from 5.41 eV (direct) due to 0.1 wt% incorporation of rGO to 5.36 eV (direct), which also decreases as a result of metal oxides incorporation to 5.23 eV (Fe_2O_3 PC), 5.27 eV (Pb_3O_4 PC) and 5.22 eV (MnO_2 PC). In other words, controlling the optical bandgap of the host matrix could be achieved via selecting the filler's type. The decrease in E_g value is mainly referred to the formed localized energy states and defects between the occupied and unoccupied molecular orbitals of the host matrix (HOMO and LUMO) as confirmed below by Urbach energy investigations [13, 17, 32]. The obtained E_g values by Tauc's method agree with those achieved by the absorption measurements. This novel conclusion is highly appreciated in a wide spectrum of optoelectronic applications. Our optical bandgap results are in accordance with the reported data [17, 34].

Investigating the formed defects in the host matrix could be achieved by exploring the Urbach energy (E_u) of the prepared plain and incorporated PCs [29, 45, 66]. The defects formed due to doping increase the amorphous character of the prepared PCs as compared with the plain one. The E_u value represents the tails' width of created energy states in the bandgap of the PCs [67, 68]. Equation 3 presents the exponential behaviour of the formed tails in the host blend. Figure 5 shows plots of ln (α) of the plain PVA and metal oxides PCs as a function of $h\nu$. The E_u values are obtained from the slopes' inverse of the fitted lines and included in Table 3. E_u value of the plain PVA is 0.21 eV, which agrees with the reported one [64, 68]. For instance, Abdullah et al. concluded that E_u of PVA increased from 0.26 to 1.28 eV due to 4 wt% of $KMnO_4$ incorporation [64]. They attributed the increment of E_u value to the created localized states in the energy bandgap of the host PVA. In addition,

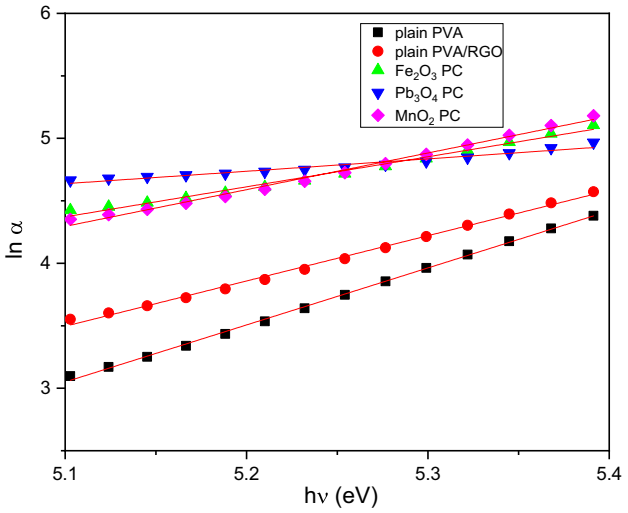

Fig. 5 ln (α) curves vs. $h\nu$ of plain PVA and metal oxides PCs

it is evident that E_u value increases to 0.28 eV (plain PVA/rGO) and more increases due to metal oxides incorporation. The E_u increment exhibits the increase in defects and voids and hence tunes the optical performance as presented above relative to the bandgap. In addition, it is clear that created defects are significantly altered as a result of the filler's type.

Moreover, the refractive index (n) is another important optical property that must be investigated for the prepared PCs to recommend their possible applications. Equation 4 shown above is used to calculate the n values of the plain PVA and metal oxides PCs. Figure 6 illustrates n plots of the plain and incorporated PCs as a function of the scanned wavelengths. It is noticed that n of the plain PVA, plain PVA/rGO and both Pb_3O_4 and MnO_2 incorporated PVA/rGO blends behaves quasi-steady in the Vis–NIR

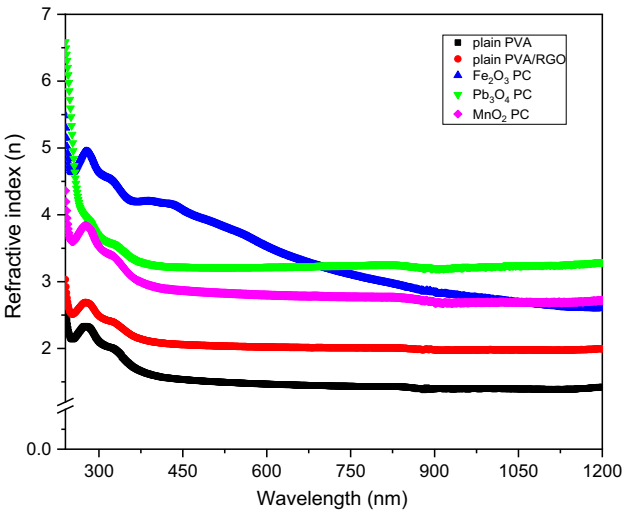

Fig. 6 Refractive index of plain PVA and metal oxides PCs

region, while n of Fe_2O_3 incorporated PVA/rGO blend decreases as λ is increased in the Vis–NIR region. In addition, at wavelength λ, n of the incorporated PCs is larger than that of the plain blend, which is larger than that of the plain PVA. These results can be interpreted in terms of the absorbance and reflectance responses caused by the filler's molecules in the host matrix [32, 69]. The metal oxides molecules work as reflecting centres as well as increase the whole density of the host matrix [70]. In addition, it is clear that the filler's quality plays a great role in controlling the refractive index of the host matrix. For example, at $\lambda = 600$ nm, n value increases from 1.45 (plain PVA) to 2.02 (plain PVA/rGO) and then to 2.79 (MnO_2 PC), 3.22 (Pb_3O_4 PC) and 3.51 (Fe_2O_3 PC). In other words, n of such a host matrix could be controlled via selecting the appropriate filler to match such applications.

The dielectric constants (real ε_r and imaginary ε_i parts) of the prepared PCs are determined as a function of $h\nu$ to endorse their probable uses. The real part of the dielectric constant presents information about the performance of the electromagnetic wave propagation through the medium and their energy-storing ability. While the imaginary part of the dielectric constant reflects the energy-loss part of the propagated electromagnetic waves [4, 18]. The calculated dielectric constants (ε_r and ε_i) using Eq.'s 7 and 8 are shown in Fig. 7a, b, respectively. It is evident that ε_r of plain and metal oxides PCs takes the trend of the refractive index n behaviour. This logical result is accepted in terms of the absorbance performance of the prepared samples. The real dielectric constant of plain PVA and Pb_3O_4 and MnO_2 incorporated PVA/rGO blends behaves quasi-steady in the Vis–NIR region, while ε_r of Fe_2O_3 incorporated PVA/rGO blend decreases as λ is increased in the Vis–NIR region. In addition, at any λ, ε_r values of the incorporated PCs are larger than that of the plain one. The increment in ε_r value is attributed to the energy density states of the incorporated PCs as compared to the plain ones. The enhancement in ε_r value of the PVA/rGO blend as well as tuning its value is highly appreciated in a lot of applications as those related to ceramics and energy storage ones. While the increase in the imaginary part of the dielectric constant as a result of incorporation is attributed to the dipole motions in the PCs [71]. The same behaviours were reported in the literature [2, 71, 72]. In instance, Soliman et al. found that the dielectric constant of PVA increased with increasing the incorporated material ($BaTiO_3$) [72]. They attributed the increments in the dielectric constants to the increase in the defects' number and the disorder nature of the PCs. Furthermore, the real energy bandgap ($E_{g\ \varepsilon i}$) of the plain PVA and metal oxides incorporated and unincorporated PVA/rGO blend could be deduced from the imaginary dielectric constant plots as illustrated in Fig. 7c. The obtained real bandgap values are also tabulated in Table 3. It is clear that the real energy ($E_{g\ \varepsilon i}$)

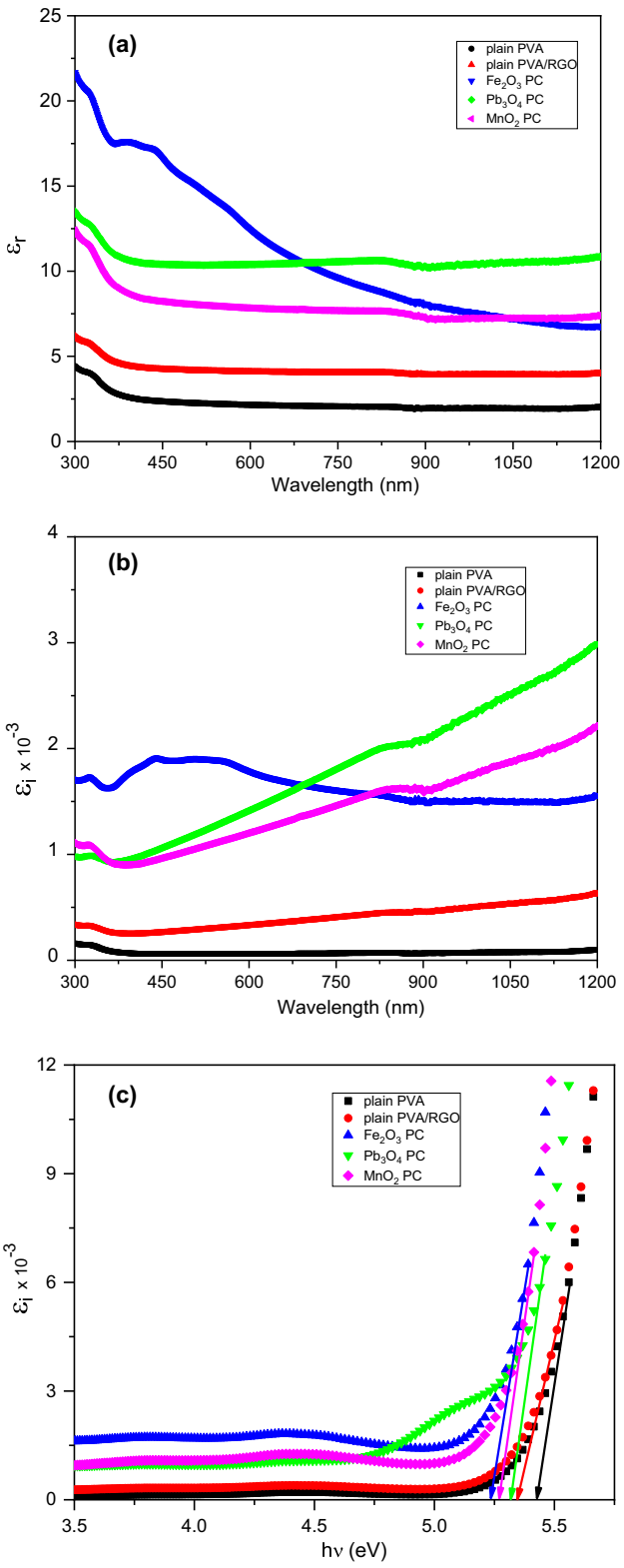

Fig. 7 Dielectric constants **a** real, **b** imaginary parts vs. wavelength and **c** imaginary parts vs. $h\nu$ of the plain PVA and metal oxides PCs

are well-matched their identical values deduced from the Tauc's relation of the direct electronic transitions [31].

Moreover, Wemple–DiDomenico (W–D) model is used to explore the effect of the filler's type on the dispersive parameters of the host blend [70]. Both the dispersive (E_d) and oscillator (E_0) energies could be investigated in the non-absorption region. The first one (E_d) reveals the transition strength, while the second one (E_0) indicates the average bandgap of the PCs [73]. Using W–D model (Eq. 9), curves of $1/(n^2-1)$ of the samples as a function of $(h\nu)^2$ are plotted (Fig. 8a), where both E_d and E_0 are deduced and listed in Table 4. According to the obtained E_d and E_0 data, a pronounced effect of the filler's type on the dispersive energies is noticed. First, the obtained E_d and E_0 of the plain PVA is well-compatible with reported [4, 7]. In addition, E_d values of the PCs are larger than that of the unincorporated blend. This result reveals that the PCs possess more inter-band transitions due to the increasing disorder character [74]. Whereas, the decrease in E_0 value of the incorporated PCs relative to the plain one is accepted based on the decrease of the optical bandgap values due to the increase in the defects density [75]. Moreover, the obtained dispersive energy findings are well-agreed with those achieved by Tauc's method as well as the reported ones [70, 75].

Besides, many other optical parameters can be determined based on the Sellmeier oscillator model and the related equations shown above (Eqs. 10–14). By plotting $1/(n^2-1)$ vs. λ^{-2} of the prepared samples as illustrated in Fig. 8b, n_∞, λ_0, S_0 and ε_∞ are estimated and also tabulated (Table 4). Furthermore, from the plots of n^2 vs. λ^2 (Fig. 8c), the values of ε_L and N/m* are obtained (Table 3). While the plasma frequency (ω_p) is calculated using Eq. 15. Noticeably, the effect of the metal oxides' incorporation on the whole optical parameters as well as its type. For example, the value of the infinite dielectric constant (ε_∞) of the metal oxides PCs is enhanced more than five times as compared with that of the plain PVA. This finding is welcomed in energy storage and supercapacitors applications. Our findings agree with the reported ones [29, 76, 77]. Our unique results introduce a valuable comparative evaluation for the optical parameters to dictate the suitable applications.

3.4 Electrical properties analysis

The dc-electrical properties performance of the plain and metal oxides PCs has been investigated to recommend their potential applications. The dc-electrical resistivity (ρ) of the samples were measured vs. temperature (300–400 K) as depicted in Fig. 9a. An obvious effect of the metal oxides type incorporation is perceived. First, ρ performance of the unincorporated PVA film agrees with the literature [5, 6]. Second, rGO blending with PVA causes a decrease in the electrical resistivity and hence an increase in the conductivity $\sigma_{dc}\left(=\frac{1}{\rho}\right)$ of the plain PVA. Similarly, the metal oxides incorporation causes an increase in the electrical

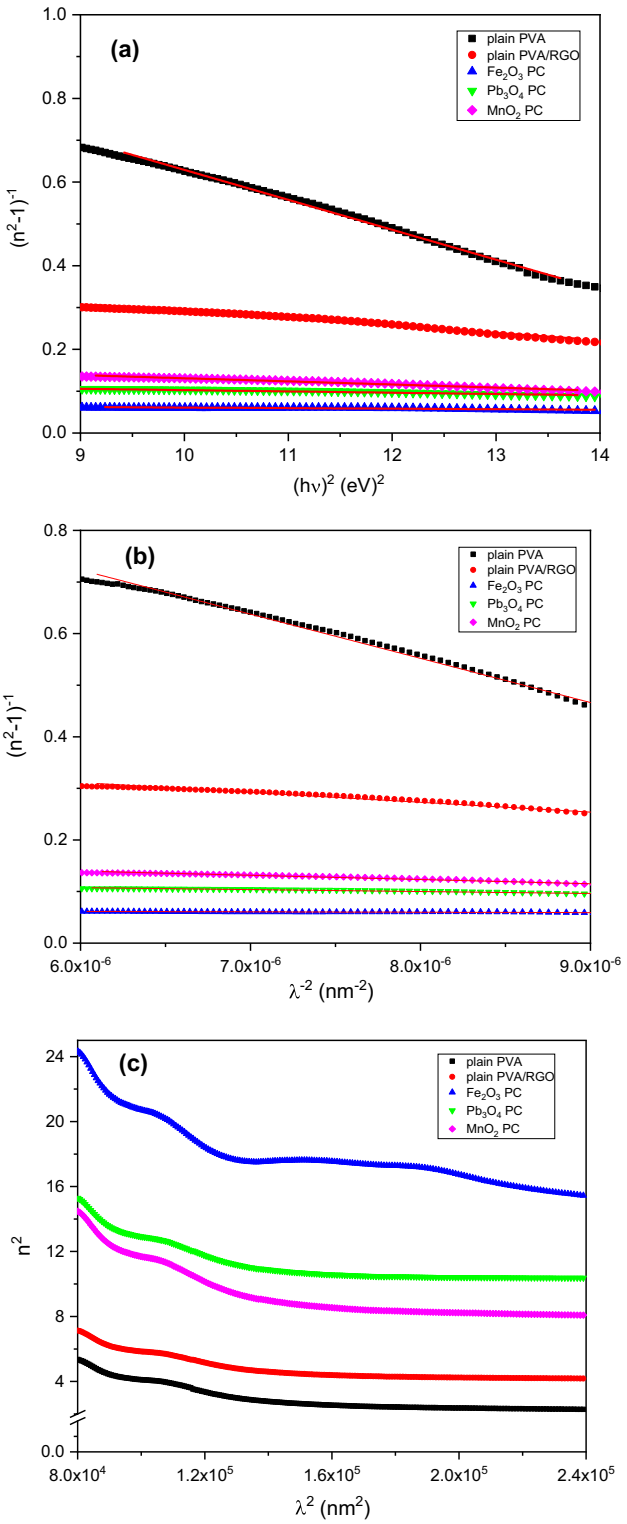

Fig. 8 Plots of **a** $1/(n^2-1)$ vs. $(h\nu)^2$, **b** $(n^2-1)^{-1}$ vs. λ^{-2} and **c** n^2 vs. λ^2 of plain and metal oxides PCs

Table 4 Optical parameters of plain PVA and metal oxides PCs

Sample	E_d (eV)	E_0 (eV)	n_∞	λ_0 (nm)	S_0 ($\times 10^{13}$m^{-2})	ε_∞	ε_L	(N/m*)$\times 10^{57}$ (kg^{-1} m^{-3})	$\omega_p \times 10^{15}$ (Hz)
plain PVA	5.17	5.22	1.35	262.8	1.18	1.81	2.71	0.98	1.02
plain PVA/rGO	11.31	5.20	1.78	333.3	2.01	3.22	4.48	1.75	1.06
Fe_2O_3 PC	51.03	4.89	2.77	186.1	19.2	7.67	19.49	1.50	1.49
Pb_3O_4 PC	32.27	5.16	2.95	175.4	25.1	8.69	10.56	9.29	1.60
MnO_2 PC	24.38	5.12	2.85	181.7	22.2	8.14	8.83	4.95	1.27

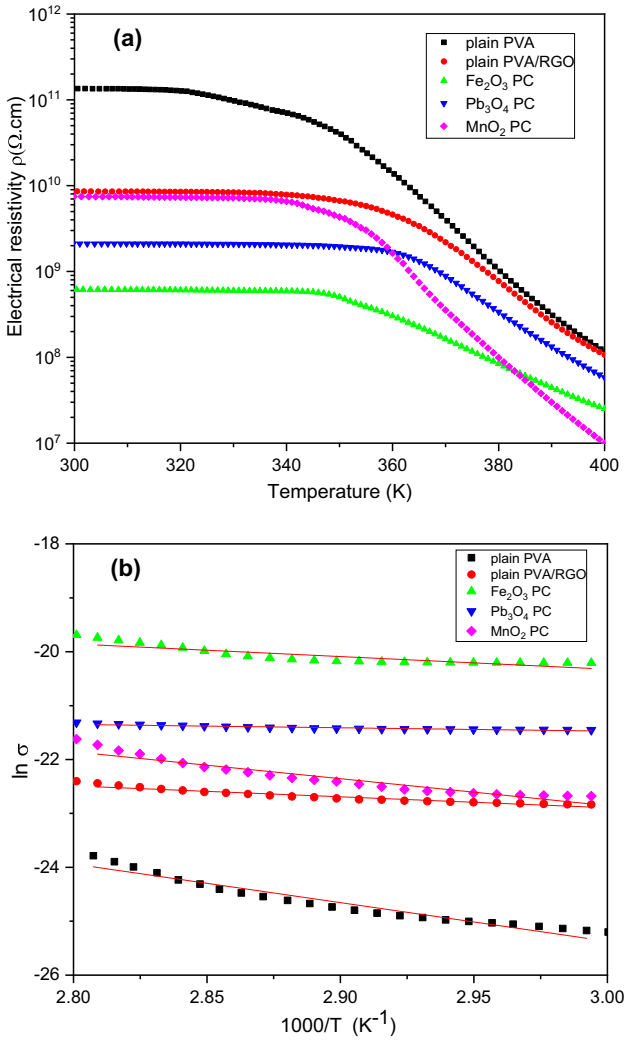

Fig. 9 **a** DC-electrical resistivity vs. temperature and **b** ln σ_{dc} vs. 1000/T of the metal oxides PCs

conductivity. This result is interpreted to the increase of the charges' carriers due to the metal oxides incorporation [78, 79]. While the decrease in ρ values as the temperature is increased and hence σ_{dc} increase of the PCs refers to the charge carriers' transferring or/and hopping within the PCs. Correspondingly, heating the PCs causes an enhancement in the polymer's chains mobility, especially with the existence of additional created defects due to the metal oxides incorporation. Moreover, the σ_{dc} performance of the prepared PCs depends on the filler's type (Table 4). For example, at 300 K, σ_{dc} value increases from 7.39×10^{-12} S cm^{-1} (plain PVA) to 1.16×10^{-10} S cm^{-1} (plain PVA/rGO). While it is enhanced to 1.62×10^{-9} S cm^{-1} (Fe_2O_3 PC) and 4.74×10^{-10} S cm^{-1} (Pb_3O_4 PC) and 1.34×10^{-10} S.cm^{-1} (MnO_2 PC). This wide variation in σ_{dc} values presents metal oxides PCs as competitive materials for applications in optoelectronic and elastic devices as well as electrolytes issues [71, 80].

Table 5 E_a and σ at 300 K of plain PVA and metal oxides incorporated and unincorporated PCs

Sample	E_a (eV)	σ at 300 K (S.cm^{-1})
plain PVA	0.66	7.39×10^{-12}
plain PVA/rGO	0.18	1.16×10^{-10}
Fe_2O_3 PC	0.05	1.62×10^{-9}
Pb_3O_4 PC	0.20	4.74×10^{-10}
MnO_2 PC	0.43	1.34×10^{-10}

Furthermore, the activation energy (E_a) of the plain PVA and metal oxides PCs has been investigated based on Arrhenius formula (Eq. 16). Figure 9b presents plots of ln σ_{dc} vs. 1000/T of the samples. The linear fits of the plotted measurements reveal their compatibility with the Arrhenius law [81, 82]. The deduced values of E_a are listed in Table 5. It is noticed that the E_a value depends on the incorporation of metal oxides' type. In addition, it is clear that the metal oxides incorporation leads to the decrease in the activation energy from 0.66 eV (plain PVA) to 0.05 eV (Fe_2O_3 incorporation). This result reveals that metal oxides incorporation causes ions migration as well as production of charges' carriers [83]. Moreover, the decrease in E_a value is caused by the bandgap shrinkage as confirmed in the optical properties analysis. Our results agree with the reported ones [83, 84].

3.5 Mechanical properties analysis

The effect of the metal oxides incorporation on the dynamic mechanical properties performance of the PVA/rGO blend has

been examined using a dynamic mechanical analyzer (DMA) in temperature swept mode. The importance of mechanical properties investigation arises due to its great role in many applications as those needed the elasticity as well as hardness natures. For example, the storage modulus (E') reflects the energy-storage ability of the sample [85]. While the loss modulus (E'') symbolizes the energy dissipated in it [86]. Figure 10a–c illustrates the storage modulus (E'), loss modulus (E'') and stiffness of plain PVA and metal oxides incorporated and incorporated PVA/rGO blend vs. temperature. A great effect on the whole mechanical properties due to the rGO blending as well as metal oxides' incorporation and their types. According to Fig. 10, each curve can be divided into three regions. The first one is called the glassy region lies from 30 °C to about 45 °C, where the quasi-stability feature is noticed. The second region lies in the temperature range from 45 °C to about 65 °C that called the glassy-leathery transition region. In the transition region, the mechanical properties are greatly altered. For example, the storage modulus and stiffness behavior decrease steeply, while the loss modulus increases sharply. However, the third region lies in the temperature region more than 70 °C, the mechanical properties return to stability character. The third region is mostly called the leathery region, where the samples are in their viscous status. Furthermore, the storage modulus, as well as the stiffness of the incorporated PCs, are enhanced as compared with the plain ones. The obtained storage modulus values at 30 °C are listed in Table 6. It is noticed that E' is duplicated due to Fe_2O_3 incorporation in PVA/rGO blend. This enhancement of the mechanical properties is attributed to the restriction feature of the host polymer chains as a result of the incorporation as compared to the plain one. As a novel result, the mechanical properties of the PVA could be enhanced via metal oxides incorporation to meet different applications in elastic stiffening devices. Comparable conclusions were accomplished in [86–88].

Moreover, the glass transition temperature (T_g) is an important thermal property that must be investigated to direct the applications of the prepared PCs in such fields. T_g is the temperature that matches the midpoint between the glassy and rubbery region of the PCs [14]. To perform that, curves of the damping factor ($\text{Tan}\delta\left(=\frac{E''}{E'}\right)$) of the samples must be plotted as a function of temperature, as shown in Fig. 11. T_g values match the maxima of the Tanδ values [89, 90]. The achieved T_g values are included in Table 6. This novel result of controlling the T_g value of the PVA polymer via incorporation with metal oxides is appreciated in many applications.

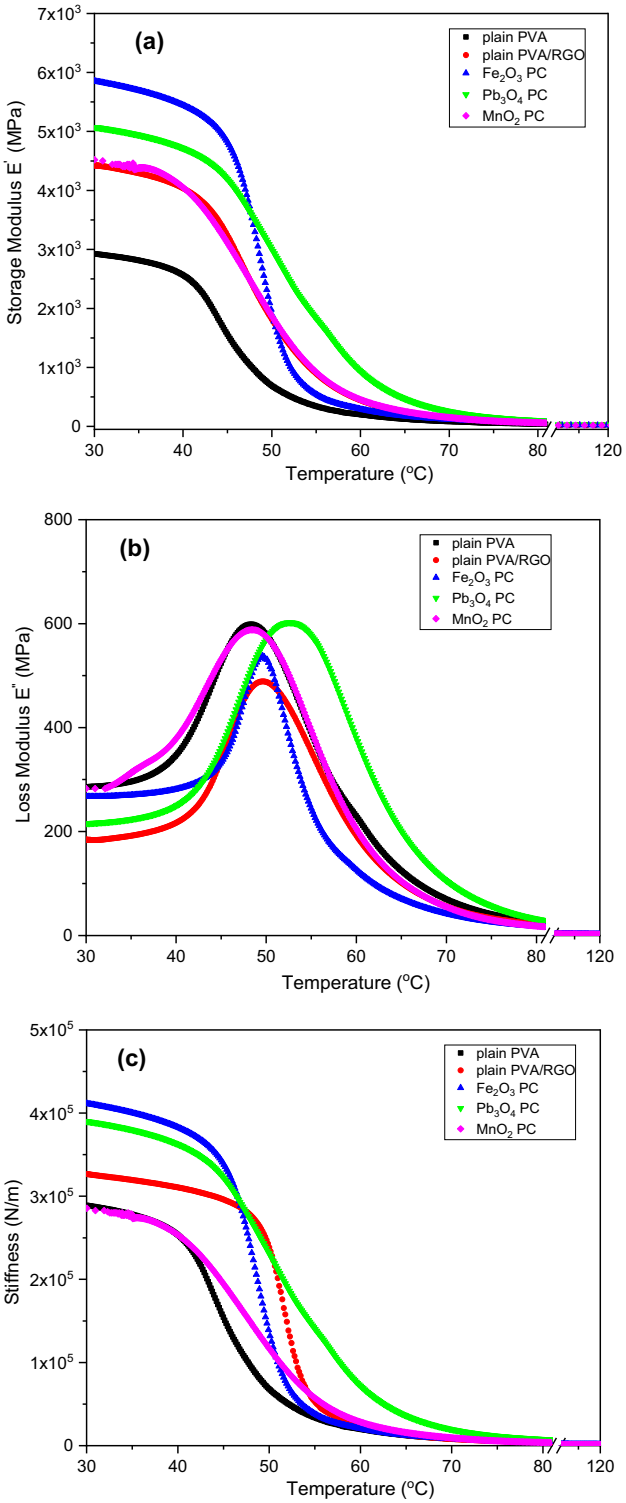

Fig. 10 **a** Storage modulus, **b** loss modulus and **c** stiffness of metal oxides PCs

Table 6 Storage modulus (E') at 30 °C and glass transition temperature (T_g) of plain PVA and metal oxides incorporated and unincorporated PCs

Sample	E' ($\times 10^3$ MPa) at 30 °C	T_g (°C)
plain PVA	2.93	59.45
plain PVA/rGO	4.46	61.56
Fe_2O_3 PC	5.94	55.04
Pb_3O_4 PC	5.08	64.68
MnO_2 PC	4.52	58.37

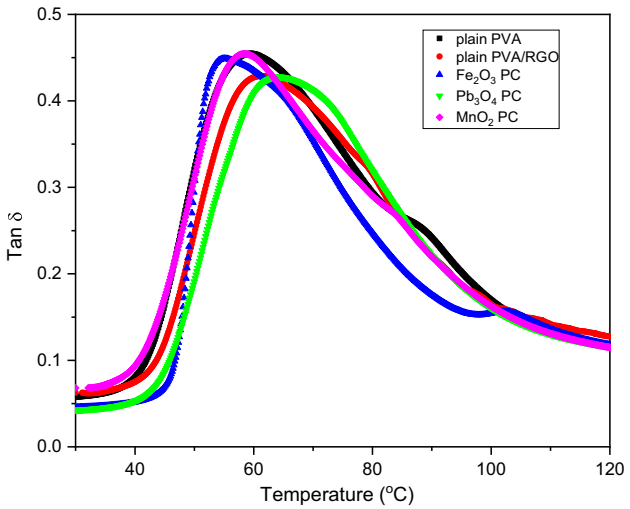

Fig. 11 Plots of Tan δ vs. temperature of metal oxides PCs

4 Conclusions

Plain PVA sample and 2.0 wt% of metal (M: Fe, Pb and Mn) oxides incorporated PVA/reduced graphene oxide polymeric composites (PVA/rGO PCs) were equipped using the solution casting procedure. Clear variations in the bands' absorption spectra have been noticed in the FT-IR spectra of the prepared samples. The effect of the metal oxide's type on the optical properties of the host PVA/rGO blend has been investigated. The energy band-gap decreases from 5.41 eV (plain PVA) to 5.36 eV (plain PVA/rGO), 5.23 eV (Fe_2O_3 PC), 5.27 eV (Pb_3O_4 PC) and 5.22 eV (MnO_2 PC). While the Urbach energy increases from 0.21 eV (plain PVA) to 0.28 eV (plain PVA/rGO), 0.41 eV (Fe_2O_3 PC), 0.64 eV (Pb_3O_4 PC) and 0.34 eV (MnO_2 PC). The refractive index (n) at 600 nm wavelength increases from 1.45 (plain PVA) to 2.02 (plain PVA/rGO) and then to 2.79 (MnO_2 PC), 3.22 (Pb_3O_4 PC) and 3.51 (Fe_2O_3 PC).The infinite dielectric constant (ε_∞) of the metal oxides PCs is enhanced more than five times as compared with that of the plain PVA. These results reveal the increase in the defects and vacancies due to the incorporation process. The dc-electrical conductivity of the PVA/rGO blend is strongly enhanced via metal oxides incorporation. The activation energy of the host matrix decreases from 0.66 eV (plain PVA) to 0.18 eV (plain PVA/rGO), 0.05 eV (Fe_2O_3 PC), 0.20 eV (Pb_3O_4 PC) and 0.43 eV (MnO_2 PC). The effect of metal oxide's type on the PVA/rGO blend mechanical properties (storage modulus, loss modulus and stiffness) and glass transition temperature has been examined. The storage modulus (E') of the plain PVA is improved from 2.93×10^3 MPa (plain PVA) to 4.46×10^3 MPa via blending with rGO. While E' of the PVA/rGO blend is enhanced to 5.94×10^3 MPa, 5.08×10^3 MPa and 4.52×10^3 MPa due to Fe_2O_3, Pb_3O_4 and MnO_2 incorporation, respectively. It is noticed that E' is duplicated due to Fe_2O_3 incorporation in PVA/rGO blend. The glass transition temperature (T_g) value increases from 59.45 °C (plain PVA) to 61.56 °C (plain PVA/rGO) and 64.68 °C (Pb_3O_4 PC). While it decreases to 55.04 °C (Fe_2O_3 PC) and 58.37 °C (MnO_2 PC). Our unique results introduce a new procedure for controlling the optical, electrical and mechanical properties of polymeric blends via metal oxides incorporation for applications in flexible optoelectronic devices.

Acknowledgements The authors thank Taif University Researchers Supporting Project number (TURSP-2020/248), Taif University, Taif, Saudi Arabia.

Declarations

Conflict of interest The authors declare no conflict of interest.

References

1. S.A.M. Issa, H.M.H. Zakaly, M. Pyshkina, M.Y.A. Mostafa, M. Rashad, T.S. Soliman, Structure, optical, and radiation shielding properties of PVA–BaTiO3 nanocomposite films: An experimental investigation. Radiat. Phys. Chem. **180**, 109281 (2021)
2. A. Badawi, Enhancement of the optical properties of PVP using Zn1-xSnxS for UV-region optical applications. Appl. Phys. A **127**(1), 51 (2021)
3. A. Badawi, S.S. Alharthi, Tailoring the photoluminescent and electrical properties of tin-doped ZnS@PVP polymeric composite films for LEDs applications. Superlattices Microstruct. **151C**, 106838 (2021)
4. Z.K. Heiba, M.B. Mohamed, A. Badawi, A.A. Alhazime, The role of Cd0.9Mg0.1S nanofillers on the structural, optical, and dielectric properties of PVA/CMC polymeric blend. Chem. Phys. Lett. **770**, 1460 (2021)
5. A. Badawi, S.S. Alharthi, A.A. Alotaibi, M.G. Althobaiti, Investigation of the mechanical and electrical properties of SnS filled PVP/PVA polymeric composite blends. J. Polym. Res. **28**(6), 205 (2021)
6. S.S. Alharthi, A. Alzahrani, M.A.N. Razvi, A. Badawi, M.G. Althobaiti, Spectroscopic and electrical properties of Ag2S/PVA

nanocomposite films for visible-light optoelectronic devices. J. Inorg. Organomet. Polym Mater. **30**(10), 3878–3885 (2020)
7. A. Badawi, Engineering the optical properties of PVA/PVP polymeric blend in situ using tin sulfide for optoelectronics. Appl. Phys. A **126**(5), 335 (2020)
8. T.A. Taha, A. Saleh, Dynamic mechanical and optical characterization of PVC/fGO polymer nanocomposites. Appl. Phys. A **124**(9), 600 (2018)
9. A. Badawi, S.S. Alharthi, M.G. Althobaiti, A.N. Alharbi, The effect of iron oxide content on the structural and optical parameters of polyvinyl alcohol/graphene nanocomposite films. J. Vinyl Addit. Technol. (2022). https://doi.org/10.1002/vnl.21889
10. K.Y. Yasoda, S. Kumar, M.S. Kumar, K. Ghosh, S.K. Batabyal, Fabrication of MnS/GO/PANI nanocomposites on a highly conducting graphite electrode for supercapacitor application. Mater. Today Chem. **19**, 100394 (2021)
11. K. Sreekanth, T. Siddaiah, N.O. Gopal, Y. Madhava Kumar, C. Ramu, Thermal, structural, optical and electrical conductivity studies of pure and Fe3+ ions doped PVP films for semoconducting polymer devices. Mater. Res. Innov. **25**(2), 95–103 (2021)
12. H.O. Tekin, S.A.M. Issa, G. Kilic, H.M.H. Zakaly, A. Badawi, G. Bilal, H.A.A. Sidek, K.A. Matori, M.H.M. Zaid, Cadmium oxide reinforced 46V2O5–46P2O5–(8–x)B2O3–xCdO semiconducting oxide glasses and resistance behaviors against ionizing gamma rays. J. Market. Res. **13**, 2336–2349 (2021)
13. A. Badawi, G.A.M. Mersal, A.A. Shaltout, J. Boman, M. Alsawat, M.A. Amin, Exploring the structural and optical properties of FeS filled graphene/PVA blend for environmental-friendly applications. J. Polym. Res. **28**(7), 270 (2021)
14. A. Badawi, S.S. Alharthi, Controlling the optical and mechanical properties of polyvinyl alcohol using Ag2S semiconductor for environmentally friendly applications. Mater. Sci. Semiconductor Process. **116**, 105139 (2020)
15. Y. Khairy, H.I. Elsaeedy, M.I. Mohammed, H.Y. Zahran, I.S. Yahia, Anomalous behaviour of the electrical properties for PVA/TiO2 nanocomposite polymeric films. Polym. Bull. **77**(12), 6255–6269 (2020)
16. S.B. Aziz, M.M. Nofal, H.O. Ghareeb, E.M.A. Dannoun, S.A. Hussen, J.M. Hadi, K.K. Ahmed, A.M. Hussein, Characteristics of poly(vinyl Alcohol) (PVA) based composites integrated with green synthesized Al3+-metal complex: structural, optical, and localized density of state analysis. Polymers **13**(8), 1316 (2021)
17. R.J. Sengwa, P. Dhatarwal, Nanofiller concentration-dependent appreciably tailorable and multifunctional properties of (PVP/PVA)/SnO2 nanocomposites for advanced flexible device technologies. J. Mater. Sci. Mater. Electron. **32**(7), 9661–9674 (2021)
18. A. Badawi, S.S. Alharthi, H. Assaedi, A.N. Alharbi, M.G. Althobaiti, Cd0.9Co01.S nanostructures concentration study on the structural and optical properties of SWCNTs/PVA blend. Chem. Phys. Lett. **775**, 1701 (2021)
19. A. Badawi, N. Al-Hosiny, S. Abdallah, The photovoltaic performance of CdS quantum dots sensitized solar cell using graphene/TiO_2 working electrode. Superlattices Microstruct. **81**, 88–96 (2015)
20. S. Ningaraju, H.B. Ravikumar, Studies on electrical conductivity of PVA/graphite oxide nanocomposites: a free volume approach. J. Polym. Res. **24**(1), 11 (2016)
21. D.-Y. Kim, B.N. Joshi, J.-J. Park, J.-G. Lee, Y.-H. Cha, T.-Y. Seong, S. In Noh, H.-J. Ahn, S.S. Al-Deyabe, S.S. Yoon, Graphene–titania films by supersonic kinetic spraying for enhanced performance of dye-sensitized solar cells. Ceram. Int. **40**(7), 11089–11097 (2014)
22. M. Aslam, M.A. Kalyar, Z.A. Raza, Synthesis and structural characterization of separate graphene oxide and reduced graphene oxide nanosheets. Mater. Res. Express **3**(10), 105036 (2016)
23. B. Mortazavi, M. Shahrokhi, M.E. Madjet, T. Hussain, X. Zhuang, T. Rabczuk, N-, B-, P-, Al-, As-, and Ga-graphdiyne/graphyne lattices: first-principles investigation of mechanical, optical and electronic properties. J. Mater. Chem. C **7**(10), 3025–3036 (2019)
24. M. Gozutok, V. Sadhu, H.T. Sasmazel, Development of poly(vinyl alcohol) (PVA)/reduced graphene oxide (rGO) electrospun mats. J Nanosci Nanotechnol **19**(7), 4292–4298 (2019)
25. P.W. Sayyad, N.N. Ingle, T. Al-Gahouari, M.M. Mahadik, G.A. Bodkhe, S.M. Shirsat, M.D. Shirsat, Selective Hg2+ sensor: rGO-blended PEDOT:PSS conducting polymer OFET. Appl. Phys. A **127**(3), 167 (2021)
26. J. Johny, S. Sepulveda-Guzman, B. Krishnan, D.A. Avellaneda, J.A. Aguilar Martinez, M.R. Anantharaman, S. Shaji, Tin sulfide: Reduced graphene oxide nanocomposites for photovoltaic and electrochemical applications. Solar Energy Mater. Solar Cells **189**, 53–62 (2019)
27. M. Aslam, M.A. Kalyar, Z.A. Raza, Graphene oxides nanosheets mediation of poly(vinyl alcohol) films in tuning their structural and opto-mechanical attributes. J. Mater. Sci. Mater. Electron. **28**(18), 13401–13413 (2017)
28. S. Mahendia, H.G. Kandhol, U.P. Deshpande, S. Kumar, Determination of glass transition temperature of reduced graphene oxide-poly(vinyl alcohol) composites using temperature dependent Fourier transform infrared spectroscopy. J. Mol. Struct. **1111**, 46–54 (2016)
29. H.M. Zidan, E.M. Abdelrazek, A.M. Abdelghany, A.E. Tarabiah, Characterization and some physical studies of PVA/PVP filled with MWCNTs. J. Market. Res. **8**(1), 904–913 (2019)
30. .-C. Cao, W. Wei, J. Liu, Q. You, F. Liu, Q. Lan, C. Zhang, C. Liu, J. Zhao, The preparation of graphene reinforced poly(vinyl alcohol) antibacterial nanocomposite thin Film. Int. J. Polym. Sci. **2015**, 407043 (2015). https://doi.org/10.1155/2015/407043
31. H. Donya, T.A. Taha, A. Alruwaili, I.B.I. Tomsah, M. Ibrahim, Micro-structure and optical spectroscopy of PVA/iron oxide polymer nanocomposites. J. Market. Res. **9**(4), 9189–9194 (2020)
32. Z.A. Alrowaili, T.A. Taha, K.S. El-Nasser, H. Donya, Significant enhanced optical parameters of PVA-Y2O3 polymer nanocomposite films. J. Inorg. Organomet. Polym Mater. **31**(7), 3101–3110 (2021)
33. Y. Khairy, M.M. Abdel-Aziz, H. Algarni, A.M. Alshehri, I.S. Yahia, H.E. Ali, The optical characteristic of PVA composite films doped by ZrO2 for optoelectronic and block UV-Visible applications. Mater. Res. Express **6**(11), 115346 (2019)
34. Z.K. Heiba, M.B. Mohamed, A.M. El-naggar, Y. Altowairqi, A.M. Kamal, Impact of ZnCdS/M (M = Co, Fe, Mn, V) doping on the structure and optical properties of PVA/PVP polymer. J. Polym. Res. **28**(12), 472 (2021)
35. E.D. Palik, *Handbook of Optical Constants of Solids* (Academic Press Handbook, New York, 1985)
36. E.M. Abdelrazek, H.M. Ragab, Spectroscopic and dielectric study of iodine chloride doped PVA/PVP blend. Indian J. Phys. **89**(6), 577–585 (2015)
37. N.M. Al-Hosiny, S.S. Alharthi, A. Badawi, Optical properties of solar irradiated Gafchromic EBT films. J. Market. Res. **14**, 1914–1920 (2021)
38. A. Badawi, M.G. Althobaiti, S.S. Alharthi, A.M. Al-Baradi, Tailoring the optical properties of CdO nanostructures via barium doping for optical windows applications. Phys. Lett. A **411**, 127553 (2021)
39. Z.K. Heiba, M.B. Mohamed, A. Badawi, N.M. Farag, Effect of sulfur deficiency on the structural, optical and electronic properties of MnS nanostructures. Chem. Phys. Lett. **779**, 138877 (2021)
40. A. Badawi, M.G. Althobaiti, Effect of Cu-doping on the structure, FT-IR and optical properties of Titania for environmental-friendly applications. Ceram. Int. **47**(8), 11777–11785 (2021)

41. A. Badawi, W.O. Al-Gurashi, A.M. Al-Baradi, F. Abdel-Wahab, Photoacoustic spectroscopy as a non-destructive technique for optical properties measurements of nanostructures. Optik **201**, 163389 (2020)
42. A. Badawi, A.H. Al Otaibi, A.M. Albaradi, N. Al-Hosiny, S.E. Alomairy, Tailoring the energy band gap of alloyed $Pb_{1-x}Zn_xS$ quantum dots for photovoltaic applications. J. Mater. Sci. Mater. Electron. **29**(24), 20914–20922 (2018)
43. J. Tauc, *Amorphous and Liquid Semiconductors* (Springer, Boston, 1974)
44. L. Dejam, S. Solaymani, A. Achour, S. Stach, Ş Ţălu, N.B. Nezafat, V. Dalouji, A.A. Shokri, A. Ghaderi, Correlation between surface topography, optical band gaps and crystalline properties of engineered AZO and CAZO thin films. Chem. Phys. Lett. **719**, 78–90 (2019)
45. A.M. Al-Baradi, F.A. Altowairqi, A.A. Atta, A. Badawi, S.A. Algarni, A.S.A. Almalki, A.M. Hassanien, A. Alodhayb, A.M. Kamal, M.M. El-Nahass, Structural and optical characteristics features of RF sputtered CdS/ZnO thin films. Chin. Phys. B **29**(8), 080702 (2020)
46. V. Dalouji, S. Elahi, S. Solaymani, A. Ghaderi, H. Elahi, Carbon films embedded by nickel nanoparticles: fluctuation in hopping rate and variable-range hopping with respect to annealing temperature. Appl. Phys. A **122**(5), 541 (2016)
47. A. Badawi, N. Al Hosiny, Dynamic mechanical analysis of single walled carbon nanotubes/polymethyl methacrylate nanocomposite films. Chin. Phys. B **24**(10), 105101 (2015)
48. M. Aslam, M.A. Kalyar, Z.A. Raza, Synthesis and structural characterization of separate graphene oxide and reduced graphene oxide nanosheets. Mater. Res. Express **3**, 105036 (2016)
49. R. Kant, D. Kumar, V. Dutta, High coercivity α-Fe2O3 nanoparticles prepared by continuous spray pyrolysis. RSC Adv. **5**(65), 52945–52951 (2015)
50. A. Ibrahim, M.H. Abdel-Aziz, M.S. Zoromba, A.F. Al-Hossainy, Structural, optical, and electrical properties of multi-walled carbon nanotubes/polyaniline/Fe3O4 ternary nanocomposites thin film. Synth. Met. **238**, 1–13 (2018)
51. T.A. Taha, M.H. Mahmoud, A. Hayat, Dielectric relaxation studies on PVC-Pb3O4 polymer nanocomposites. J. Mater. Sci. Mater. Electron. **32**(23), 27666–27675 (2021)
52. S.A. Mansour, A.H. Farha, M.F. Kotkata, Sol–gel synthesized Co-doped anatase TiO2 nanoparticles: structural, optical, and magnetic characterization. J. Inorg. Organomet. Polym Mater. **29**(4), 1375–1382 (2019)
53. A. El Mragui, Y. Logvina, L. Pinto da Silva, Synthesis of Fe- and Co-doped TiO(2) with improved photocatalytic activity under visible irradiation toward carbamazepine degradation. Materials **12**(23), 3874 (2019)
54. M.T. Rahman, M.A. Hoque, G.T. Rahman, M.M. Azmi, M.A. Gafur, R.A. Khan, M.K. Hossain, Fe2O3 nanoparticles dispersed unsaturated polyester resin based nanocomposites: effect of gamma radiation on mechanical properties. Radiat. Eff. Defects Solids **174**(5–6), 480–493 (2019)
55. F.M. Ali, R.M. Kershi, M.A. Sayed, Y.M. AbouDeif, Evaluation of structural and optical properties of Ce3+ ions doped (PVA/PVP) composite films for new organic semiconductors. Phys. B **538**, 160–166 (2018)
56. Y. Khairy, I.S. Yahia, H. Elhosiny Ali, Facile synthesis, structure analysis and optical performance of manganese oxide-doped PVA nanocomposite for optoelectronic and optical cut-off laser devices. J. Mater. Sci. Mater. Electron. **31**(10), 8072–8085 (2020)
57. R.F. Bhajantri, V. Ravindrachary, B. Poojary, I.A. Harisha, V. Crasta, Studies on fluorescent PVA + PVP + MPDMAPP composite films. Polym. Eng. Sci. **49**(5), 903–909 (2009)
58. S. Rajendran, M. Sivakumar, R. Subadevi, Investigations on the effect of various plasticizers in PVA–PMMA solid polymer blend electrolytes. Mater. Lett. **58**(5), 641–649 (2004)
59. M. Irfan, A. Manjunath, S.S. Mahesh, R. Somashekar, T. Demappa, Influence of NaF salt doping on electrical and optical properties of PVA/PVP polymer blend electrolyte films for battery application. J. Mater. Sci. Mater. Electron. **32**(5), 5520–5537 (2021)
60. S. Muntaz Begum, K. Ravindranadh, R.V.S.S.N. Ravikumar, M.C. Rao, Structural and luminescent properties of PVA capped ZnSe nanoparticles. Mater. Res. Innov. **22**(1), 37–42 (2018)
61. N.H.A. Ngadiman, A. Idris, M. Irfan, D. Kurniawan, N.M. Yusof, R. Nasiri, γ-Fe2O3 nanoparticles filled polyvinyl alcohol as potential biomaterial for tissue engineering scaffold. J. Mech. Behav. Biomed. Mater. **49**, 90–104 (2015)
62. A. Sankhla, R. Sharma, R.S. Yadav, D. Kashyap, S.L. Kothari, S. Kachhwaha, Biosynthesis and characterization of cadmium sulfide nanoparticles—an emphasis of zeta potential behavior due to capping. Mater. Chem. Phys. **170**, 44–51 (2016)
63. R.F. Bhajantri, V. Ravindrachary, A. Harisha, V. Crasta, S.P. Nayak, B. Poojary, Microstructural studies on BaCl2 doped poly(vinyl alcohol). Polymer **47**(10), 3591–3598 (2006)
64. O.G. Abdullah, S.B. Aziz, M.A. Rasheed, Structural and optical characterization of PVA:KMnO4 based solid polymer electrolyte. Results Phys. **6**, 1103–1108 (2016)
65. S.B. Aziz, Modifying poly(Vinyl Alcohol) (PVA) from insulator to small-bandgap polymer: a novel approach for organic solar cells and optoelectronic devices. J. Electron. Mater. **45**(1), 736–745 (2016)
66. M. Rashad, H.A. Saudi, H.M.H. Zakaly, S.A.M. Issa, A.M. Abd-Elnaiem, Control optical characterizations of Ta+5–doped B2O3–Si2O–CaO–BaO glasses by irradiation dose. Opt. Mater. **112**, 110613 (2021)
67. S. Choudhary, R.J. Sengwa, ZnO nanoparticles dispersed PVA–PVP blend matrix based high performance flexible nanodielectrics for multifunctional microelectronic devices. Curr. Appl. Phys. **18**(9), 1041–1058 (2018)
68. P. Dhatarwal, R.J. Sengwa, Investigation on the optical properties of (PVP/PVA)/Al2O3 nanocomposite films for green disposable optoelectronics. Phys. B Condens. Matter **613**, 412989 (2021)
69. A.M. El Sayed, W.M. Morsi, α-Fe2O3 /(PVA + PEG) Nanocomposite films; synthesis, optical, and dielectric characterizations. J. Mater. Sci. **49**(15), 5378–5387 (2014)
70. O.G. Abdullah, S.B. Aziz, K.M. Omer, Y.M. Salih, Reducing the optical band gap of polyvinyl alcohol (PVA) based nanocomposite. J. Mater. Sci. **26**(7), 5303–5309 (2015)
71. Y. Khairy, M.I. Mohammed, H.I. Elsaeedy, I.S. Yahia, Optical and electrical properties of SnBr 2-doped polyvinyl alcohol (PVA) polymeric solid electrolyte for electronic and optoelectronic applications. Optik **228**, 166129 (2021)
72. T.S. Soliman, M.F. Zaki, M.M. Hessien, S.I. Elkalashy, The structure and optical properties of PVA-BaTiO3 nanocomposite films. Optical Mater. **111**, 110648 (2020)
73. A. Badawi, Engineering the energy bandgap of lead cobalt sulfide quantum dots for visible light optoelectronics. J. Mater. Sci. Mater. Electron. **31**, 17726–17735 (2020)
74. Z.K. Heiba, M.B. Mohamed, Effect of annealed and Mg-doped nano ZnO on physical properties of PVA. J. Mol. Struct. **1181**, 507–517 (2019)
75. J.Q.M. Almarashi, M.H. Abdel-Kader, Exploring nano-sulfide enhancements on the optical, structural and thermal properties of polymeric nanocomposites. J. Inorg. Organomet. Polym Mater. **30**(8), 3230–3240 (2020)
76. R. Nangia, N.K. Shukla, A. Sharma, Optical and structural properties of Se80Te15Bi5/PVA nanocomposite films. J. Mol. Struct. **1177**, 323–330 (2019)

77. T.H. AlAbdulaal, H.E. Ali, V. Ganesh, A.M. Aboraia, Y. Khairy, H.H. Hegazy, A.V. Soldatov, H.Y. Zahran, M.S. Abdel-wahab, I.S. Yahia, Investigating NaIO3 doped PVA polymeric nanocomposites via the structural morphology and linear and nonlinear optical analysis: For optoelectronic systems. Optik **245**, 167724 (2021)
78. A.M. Ibrahim, H.I. Alkhammash, Influence of extra-addition of sulfur on the optical, electrical, and photoconductivity of the borate glasses containing MoO3. J. Mater. Sci. Mater. Electron. **32**, 7294–7306 (2021)
79. Z.K. Heiba, M.B. Mohamed, A. Badawi, Structure, optical and electronic characteristics of iron-doped cadmium sulfide under nonambient atmosphere. Appl. Phys. A **127**(3), 166 (2021)
80. N. Ahad, E. Saion, E. Gharibshahi, Structural, thermal, and electrical properties of PVA-sodium salicylate solid composite polymer electrolyte. J. Nanomater. **2012**, 857569 (2012). https://doi.org/10.1155/2012/857569
81. M. Watanabe, K. Sanui, N. Ogata, F. Inoue, T. Kobayashi, Z. Ohtaki, Temperature dependence of ionic conductivity of crosslinked Poly(propylene oxide) films dissolving lithium salts and their interfacial charge transfer resistance in contact with lithium electrodes. Polym. J. **16**(9), 711–716 (1984)
82. S. Ramesh, A.H. Yahaya, A.K. Arof, Dielectric behaviour of PVC-based polymer electrolytes. Solid State Ionics **152–153**, 291–294 (2002)
83. M. Ravi, S. Bhavani, K. Kiran Kumar, V.V.R. Narasimaha Rao, Investigations on electrical properties of PVP:KIO4 polymer electrolyte films. Solid State Sci. **19**, 85–93 (2013)
84. N.M. Al-Hosiny, S. Abdallah, M.A.A. Moussa, A. Badawi, Optical, thermophysical and electrical characterization of PMMA (CdSe QDs) composite films. J. Polym. Res. **20**(2), 1–8 (2013)
85. K. Sewda, S.N. Maiti, Dynamic mechanical properties of high density polyethylene and teak wood flour composites. Polym. Bull. **70**, 2657–2674 (2013)
86. A. Badawi, Characterization of the optical and mechanical properties of CdSe QDs/PMMA nanocomposite films. J. Mater. Sci. Mater. Electron. **26**(6), 3450–3457 (2015)
87. N.G. Sahooa, S. Ranab, J.W. Chob, L. Li, S.H. Chana, Polymer nanocomposites based on functionalized carbon nanotubes. Prog. Polym. Sci. **35**, 837–867 (2010)
88. Y.-L. Huang, C.-C.M. Ma, S.-M. Yuen, C.-Y. Chuang, H.-C. Kuan, C.-L. Chiang, S.-Y. Wu, Effect of maleic anhydride modified MWCNTs on the morphology and dynamic mechanical properties of its PMMA composites. Mater. Chem. Phys. **129**(3), 1214–1220 (2011)
89. A. Montazeri, K. Pourshamsian, M. Riazian, Viscoelastic properties and determination of free volume fraction of multi-walled carbon nanotube/epoxy composite using dynamic mechanical thermal analysis. Mater. Des. **36**, 408–414 (2012)
90. V. Mathur, M. Dixit, K.S. Rathore, N.S. Saxena, K.B. Sharma, Morphological and mechanical characterization of a PMMA/CdS nanocomposite. Front. Chem. Sci. Eng. **5**(2), 258–263 (2011)